metals

MDPI

Article

Comparative Study of (Fe,Nb)MoTaTiZr High Entropy Alloys in Ringer Grifols Solution

Miguel Lopez-Rios [1], Santiago Brito-Garcia [1], Julia Mirza-Rosca [1,2,*] and Ionelia Voiculescu [3]

[1] Mechanical Engineering Department, University of Las Palmas de Gran Canaria, 35001 Las Palmas de Gran Canaria, Spain
[2] Materials Engineering and Welding Department, Transilvania University of Brasov, 500036 Brasov, Romania
[3] Quality Engineering and Industrial Technologies Department, Faculty of Industrial Engineering and Robotics, National University of Science and Technology Politehnica of Bucharest, 060042 Bucharest, Romania
* Correspondence: julia.mirza@ulpgc.es

Abstract: High-entropy alloys (HEAs) are a family of materials that, because of their particular characteristics and possible uses in a variety of industries, have garnered a lot of interest recently. One such promising HEA is the MoNbTaTiZr high-entropy alloy, which displays excellent corrosion resistance and biocompatibility alongside good mechanical properties. Another promising HEA that has attracted researchers for its potential applications in various fields is FeMoTaTiZr. Exchanging one of the elements may result in important variation of properties of a material. This work studies two different samples of high-entropy alloys, MoNbTaTiZr (named NbHEA) and FeMoTaTiZr (named FeHEA), both generated in a laboratory context using electric-arc remelting technology, keeping similar atomic percentage of the elements in both alloys. Optical microscopy and scanning electron microscopy techniques were used to characterize the microstructure of the alloys. Replacing Nb for Fe affects the distribution proportion of the other four elements, since Fe has a higher tendency than Nb to form part of the inter-dendrite region. An evaluation of the properties related to the corrosion process was accomplished using the polarization method along with electrochemical impedance spectroscopy (EIS), performed under a simulated biological environment. As a result, FeHEA showed a higher corrosion rate in simulated body fluid than NbHEA.

Keywords: high-entropy alloys; corrosion resistance; microstructure; microscopy; biomaterial; EIS

Citation: Lopez-Rios, M.; Brito-Garcia, S.; Mirza-Rosca, J.; Voiculescu, I. Comparative Study of (Fe,Nb)MoTaTiZr High Entropy Alloys in Ringer Grifols Solution. *Metals* **2024**, *14*, 1430. https://doi.org/10.3390/met14121430

Academic Editors: Yonggang Yao and Yong Zhang

Received: 20 November 2024
Revised: 10 December 2024
Accepted: 11 December 2024
Published: 13 December 2024

1. Introduction

Conventional alloys consist mainly of a principal element acting as a matrix where other elements are included to improve the properties of the material, giving rise to an alloy based on the main element. Classic metallic alloys are often made with one metal in a large proportion, known as the base metal, and small amount of other elements, though some alloys with two metals in similar quantities can be discovered. These other elements, even in small proportions, can entail important differences in the characteristics of the resulting material.

The traditional approach to alloy development has been extremely limited in its ability to explore the entire spectrum of potential alloys [1]. A relatively fresh class of materials, HEAs have drawn plenty of concern in materials research and engineering since their discovery in the early 2000s. Unlike traditional alloys, several main components are present in HEAs in about equal concentrations. The development of HEAs over the last 10 years has provided fresh impetus for the study of novel materials intended for high-performance applications [2], considering that the arrangement of different atomic species in HEAs can offer several advantages compared to single element-based alloys.

Yeh [3] proposed in 2006 that four core effects could be proposed to characterize the behavior of HEAs: high-entropy, sluggish diffusion, severe lattice distortion, and "cocktail" effects. One accepted and usually used definition for HEAs describes them as

alloys comprising five or more elements in a compositional range of 5–35 at % each. These elements tend to form a single solid-solution phase. However, other stipulations can be read in the literature extending the range of multicomponent alloys over single-phase formation. Some of those expressions are multiprincipal element alloys (MPEAs), complex concentrated alloys (CCAs), and high-entropy materials (HEMs) [4,5].

Orthopedic implants have been mainly based in titanium alloys due to their biocompatibility and corrosion resistance of the passive film formed on the surface [6]. For example, a recent study advances the use of Ti-Mo-based materials because of the cytocompatibility and enhanced osseointegration [7,8]. The future of medical improvements is to be accompanied by a new generation of metallic biomaterials showing superior mechanical properties and higher biocompatibility, a combination that can be found in the new high-entropy alloys.

Since the component elements of Ti-rich Ti-Nb-Ta-Zr (TNTZ) alloys with a bcc phase are non-toxic and allergy-free, they have been studied as improved Ti-based metallic biomaterials [9]. The combination of Ta, Nb, Mo, Zr, and Ti promotes the development of a single solid solution phase in HEAs [10]. The formation of a solid solution gives rise to deformability and a severely distorted lattice. After Senkov et al. [11] introduced refractory HEAs featuring a solitary bcc phase in W-Nb-Mo-Ta and W-Nb-Mo-Ta-V alloy systems, researchers analyzed other bcc HEAs by incorporating early transition metals, such as zirconium [12]. The ions of zirconium, niobium, and tantalum that are released are titanium-like ions and do not typically exhibit toxicity when interacting with biomolecules. This is because the active ions readily bond with a nearby water molecule or an anion to create an oxide, hydroxide, or inorganic salt [13].

Some studies of both equiatomic and non-equiatomic MoNbTaTiZr HEA have been developed in the past recent years [14,15] as a consequence of the biomaterial concept of the alloy, but there are still many composition and fabrication possibilities to investigate. The Mo-Nb-Ta-Ti-Zr system alloy recipes were based on the choice of chemical elements with low bio-toxicity for the human body [16], which are currently being tested both for the manufacture of surgical instruments and for orthopedic applications [17]. The excellent biocompatibility of HEAs MoNbTaTiZr places these alloys as a new class of metallic biomaterials showing exceptional characteristics. For this reason, a new high-entropy alloy was obtained with iron in place of niobium, FeMoTaTiZr, taking into account that the iron does not tend to accumulate in tissues being metabolized [18].

In this work, two non-equiatomic MoNbTaTiZr and FeMoTaTiZr HEA, both being produced in an electric-arc remelting furnace, are tested for microstructure characterization and corrosion resistance behavior under a simulated physiological environment. Most of the elements that compose these alloys are refractory, so in order to ensure a better dissolution in the molten matrix and a better homogeneity of the alloy, Nb, which has a high melting point (2477 °C), was substituted with Fe (1538 °C), a component that is additionally essential in the human body.

2. Materials and Methods

2.1. Materials and Samples Preparation

The MoNbTaTiZr and FeMoTaTiZr high-entropy alloys (named NbHEA and Fe-HEA, respectively) were produced in an MRF ABJ 900 Vacuum Arc Remelting (VAR) furnace(Allenstown, NH, USA). Elements with a purity of at least 99.0% were utilized as raw materials, including Fe, Mo, Ta, Nb, Ti, and Zr (see Table 1).

The raw materials, melted and mixed under the action of the electric arc, were then cooled to be flipped and re-melted for 8 times under an argon atmosphere, in order to homogenize the distribution of the different elements, since the sample contained high melting temperature elements such as Nb (2477 °C), Mo (2623 °C), and Ta (3017 °C), compared to Fe (1538 °C), Ti (1668 °C), and Zr (1855 °C).

Table 1. NbHEA and FeHEA samples composition in atomic and weight percentage.

Element	wt %		at %	
	FeHEA	**NbHEA**	**FeHEA**	**NbHEA**
Mo	20.45	17.32	18.66	17.98
Ta	32.45	38.95	15.71	21.45
Ti	12.67	13.21	23.18	27.49
Zr	18.97	17.45	18.21	19.06
Fe	15.46	-	24.24	-
Nb	-	13.07	-	14.02

The obtained ingots had a mass of approximately 30 g (+/−0.2 g) and dimensions of 25 × 9 mm. The ingots were cut using an abrasive disk under cooling liquid jet and then embedded into an epoxy resin cylinder. The exposed surface of the NbHEA sample out of the resin is 0.652 cm^2, whereas for the FeHEA sample, the exposed surface is 0.695 cm^2. Preparation for the metallographic test was performed using abrasive paper with grit sizes between 240 and 2000 and then alpha alumina suspension of 3 µm and 0.1 µm. Finally, the surface was cleansed with deionized water using an ultrasonic cleaning system, consistent with ASTM E3-11(2017) [19].

2.2. Microstructural Characterization

To examine the sample's surface, Kroll reactive solution was used for etching. The OLYMPUS PME 3—ADL microscope (Olympus Corp., Tokyo, Japan) was then utilized to make observations.

The phase analysis was characterized using the Bruker D8 ADVANCE diffractometer (Billerica, MA, USA) to measure the X-ray diffraction data of the samples. This study was conducted using CuKα radiation (λ = 1.5418 Å) in Bragg–Brentano geometry with a step size of 0.02° and a power of 40 kV (LYNXEYE XE high-speed position-sensitive detector, Billerica, MA, USA) in the range of 2θ = 5–80°.

Additionally, the alloy was analyzed using a scanning electron microscope FE-SEM Zeiss Sigma 300 VP (Carl Zeiss, Jena, Germany), equipped with an energy dispersive X-ray spectrometer (Edax Inc., Mahwah, NJ, USA). The SEM micrographs were acquired in high-vacuum mode. A cathode voltage of 25 kV was used, keeping a working distance of 10 mm. A backscattered electron detector (BSD) along with a Z contrast revealed the different phases within the sample.

2.3. Electrochemical Measurements

Electrochemical measurement is one effective analytical technique for corrosion investigation. An electrochemical cell with three electrodes was employed. A saturated calomel electrode (SCE) served as the reference electrode. The working electrode was the HEA sample, whereas Pt was the counter electrode. The electrolyte was Ringer Grifols composed of (values in mmol/L): Na^+ 129.9; K^+ 5.4; Ca^{2+} 1.8; Cl^- 111.7; $C_3H_5O_3^-$ 27.2. Essays were performed at 37 ± 0.1 °C using a thermostatic bath. A computer with EC-Lab® software 9.55 package together with a SP-150 potentiostate (Biologic Science Instruments, Seyssinet-Pariset, France) was in the support tool for the experiment.

The open circuit potential was measured during 24 h. Then, potentiodynamic polarization measurements were registered. OCP provides qualitative findings regarding the state of corrosion but provides no information regarding the rate of corrosion.

The polarization curve can be used to determine the corrosion potential, whereas the Tafel slope can be used to fix the corrosion rate. Tafel slopes for both anodic processes (b_a) and cathodic processes (b_c) were calculated shifting linear polarization curves. The ASTM G 5-87 Standard Reference Test Method for Making Potentiostatic and Potentiodynamic Anodic Polarization Measurements was followed in varying the samples' potential throughout a range of values [20]. Current through the electrode is then monitored during

the scanning of potential values. A scan rate of 300 µV/1807 ms was the pattern for the potentiodynamic polarization accomplished [21].

The EIS experiment used a sinusoidal round potential E, set to the constant value of the open circuit potential to perform impedance testing into potentiostatic arrangement [22]. The cell current was stabilized after 24 h open circuit potential test. Scanning from 100 kHz to 100 mHz and an amplitude of 10 mV from peak to peak was carried out.

2.4. Microhardness

An indentation test was performed at 25 °C and 45% humidity. The equipment used was a Shimadzu HMV 2T microhardness tester (Shimadzu, Kyoto, Japan) to ascertain the microhardness of the samples. Before taking perpendicular microhardness measurements, the sample was previously polished to a mirror finish, and then viewed under an optical microscope. Following the diameter of the sample, indentations were made at intervals of 0.5 mm, with a low load of 9.1 mN (1 gf). A dwelling time of 10 s was performed for the loads. Up to ten indentations were produced for every sample, based on ISO 14577-1:2015 [23]. From these values, the Vickers hardness (HV) was computed for each sample.

3. Results and Discussions

3.1. Microstructural Characterization

The microstructure of the FeHEA and NbHEA can be observed through the optical microscopy of the two samples at 20× magnification in Figure 1. In both cases, grain microstructure is observed. The composing elements' distribution through solidification may result in the creation of a dendrite phase (light grey contrast in the images) and an inter-dendrite phase (dark grey contrast in the images).

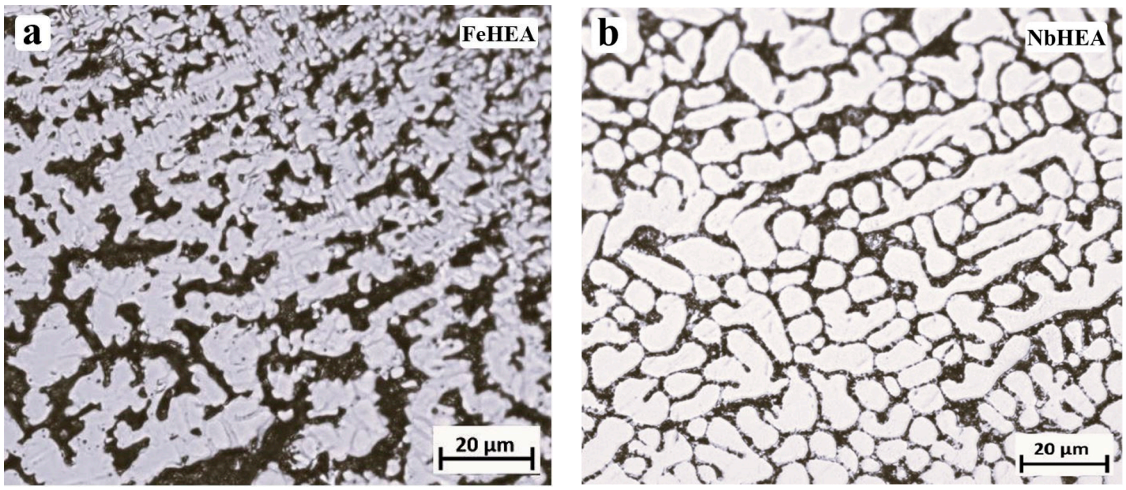

Figure 1. Optical microscopy at 20× magnification of (**a**) FeHEA microstructure and (**b**) NbHEA microstructure.

X-ray diffraction (XRD) analyses were performed, and the data obtained were subjected to Rietveld refinement processing using the TOPAS V6 program.

Factors R_p and R_{wp} are defined as follows:

$$R_p = \frac{\sum |Y_i(obs) - Y_i(calc)|}{\sum Y_i(obs)} \quad (1)$$

$$R_{wp} = \left\{ \frac{\sum w_i [Y_i(obs) - Y_i(calc)]^2}{\sum w_i [Y_i(obs)]^2} \right\}^{\frac{1}{2}} \quad (2)$$

Table 2 illustrates the resulting lattice parameters after refinement, as well as after Rietveld refinement analysis, for the MoNbTaTiZr sample.

Table 2. Lattice parameters and Rietveld refinement results for the MoNbTaTiZr alloy.

Phase	Lattice Parameters (Å)			Crystallite Size (nm)	Mass Proportion (%)	Space Group	Reliability Factors		
	a	b	c				R_p	R_{wp}	R_{exp}
MoNbTa	3.24 (9)			16 (1)	16.36	Im-3m (229) (bcc)	7.85	10.94	1.92
Ti_4Nb	3.19 (8)	4.87 (5)	4.60 (7)	102 (2)	3.80	Cmcm (orthorombic)			
Ta	2.82 (9)		5.34 (5)	16 (6)	74.22	P63/m (hexagonal)			
$Ti_{0.879}Nb_{0.121}$	3.11 (9)	5.09 (7)	4.62 (1)	81 (1)	5.62	Cmcm (orthorombic)			

The results obtained from the Rietveld analysis indicated the presence of Ta as the main phase, crystallized in the hexagonal system. Alongside it, in smaller proportions, MoNbTa solid solution appears, crystallized in the BCC system, and the compounds $Ti_{0.879}Nb_{0.121}$ and Ti_4Nb, both crystallized in the orthorhombic system.

Table 3 illustrates the resulting lattice parameters after refinement, as well as after Rietveld refinement analysis, for the FeMoTaTiZr sample.

Table 3. Lattice parameters and Rietveld refinement results for the FeMoTaTiZr alloy.

Phase	Lattice Parameters (Å)			Crystallite Size (nm)	Mass Proportion (%)	Space Group	Reliability Factors		
	a	b	c				R_p	R_{wp}	R_{exp}
Ti_2Fe	11.336 (14)			26.7 (27)	39.63	Fd-3m (fcc)	5.18	8.37	1.68
MoTa	3.2093 (40)			38.3 (51)	23.40	Im-3m (bcc)			
Mo	3.1421 (39)			28.2 (25)	20.68	Im-3m (bcc)			
(Fe Mo) Zr	5.2103 (64)		8.502 (11)	28.7 (15)	16.13	P63/mmc (hexagonal)			
Ti_7Zr_3	2.989 (20)		4.683 (97)	70 (16)	0.16	P63/mmc (hexagonal)			

These results indicated the presence of three main phases, crystallized in the cubic system: Ti_2Fe, MoTa, and Mo. In addition to these three main constituents, small proportions of solid phase (Fe Mo) Zr and Ti_7Zr_3 compound were also identified.

Mitsuharu Todai et al. [10] have published SEM-back scattering electron images of the MoNbTaTiZr HEA, both as-cast and annealed samples. Also, X-ray diffraction results for MoNbTaTiZr HEA are published by Takao Hori et al. [24]. Those XRD patterns of MoNbTaTiZr alloy showed a main bcc phase and a minor bcc phase (with a different lattice constant), and no indication of any intermetallic compound phases or bcc-based ordered phases. The annealing in Todai's study did not lead the decomposition of bcc solid solution phases to other phases, concluding that the formation of bcc HEA keeps a high phase stability [10]. The review on HEAs as biomaterials shows that the vast majority have a bcc structure [25].

SEM images of the MoNbTaTiZr sample at higher magnification, along with EDS graphs, are shown in Figure 2. Composition of elements in the dendrite and interdendrite regions have been aimed, performing EDS analyses on micro-zones with the same area. The results of the global and punctual chemical composition for the samples are presented in Table 4.

SEM images of FeHEA at the same magnification as for NbHEA and their respective EDS graphs are presented in Figure 3. In the same way as with the previous alloy, EDS analyses are used to obtain composition of elements both in the dendrite and interdendrite regions. The chemical composition for the different points is exposed in Table 5.

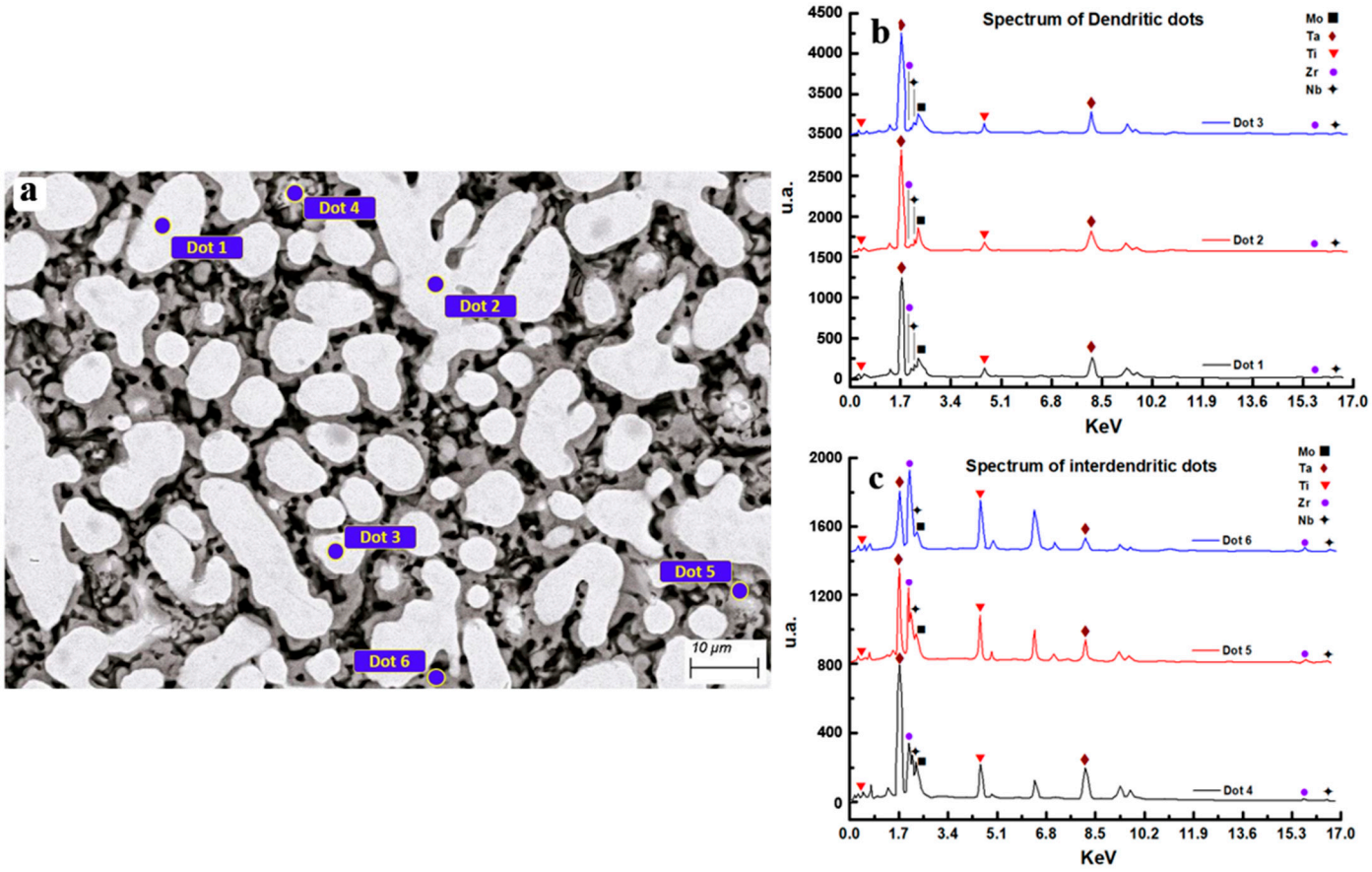

Figure 2. (**a**) SEM and EDS analysis for Area 1, Area 2, and Area 3 of MoNbTaTiZr high-entropy alloy; (**b**) compositional spectrum in dendritic areas; (**c**) compositional spectrum in interdendritic areas.

Table 4. EDS quantification results of atomic and weight percentage on dendritic (D) and interdendritic (ID) microstructures of MoNbTaTiZr high-entropy alloy.

Spot	1		2		3		4		5		6	
	D		D		D		ID		ID		ID	
Elements	**wt %**	**at %**	**wt %**	**at %**	**wt %**	**at %**	**wt %**	**at %**	**wt %**	**at %**	**wt %**	**at %**
Ti	6.20	15.74	5.89	14.99	6.21	15.84	10.46	23.53	14.26	28.48	19.94	36.16
Zr	3.66	4.88	4.04	5.41	3.72	4.98	20.74	24.49	31.30	32.82	39.60	37.70
Nb	10.68	13.97	9.07	11.91	9.87	12.97	9.80	11.36	10.23	10.53	9.04	8.45
Mo	20.30	25.71	21.90	27.85	20.25	25.76	11.60	13.03	10.24	10.21	6.11	5.53
Ta	59.15	39.71	59.10	39.85	59.95	40.45	39.52	23.53	33.97	17.96	25.32	12.16

Attending to compositions obtained, segregation factor is calculated for every element in both NbHEA and FeHEA. This factor is a parameter that helps to evaluate the segregation degree of an alloy and that facilitates comparison between the different elements for those two alloys. The segregation factor relates element concentration in the dendritic compared to the interdendritic area, following the formula:

$$S_R = \frac{\text{Element concentration in Dendritic area}}{\text{Element concentration in Interdendritic area}} \quad (3)$$

The results are shown in Table 6. Both dendrite and inter-dendrite regions contain all the constituent elements, but whereas Mo and Ta show a tendency towards the dendrite region, Ti, Zr, and Fe have an inclination to the inter-dendrite region.

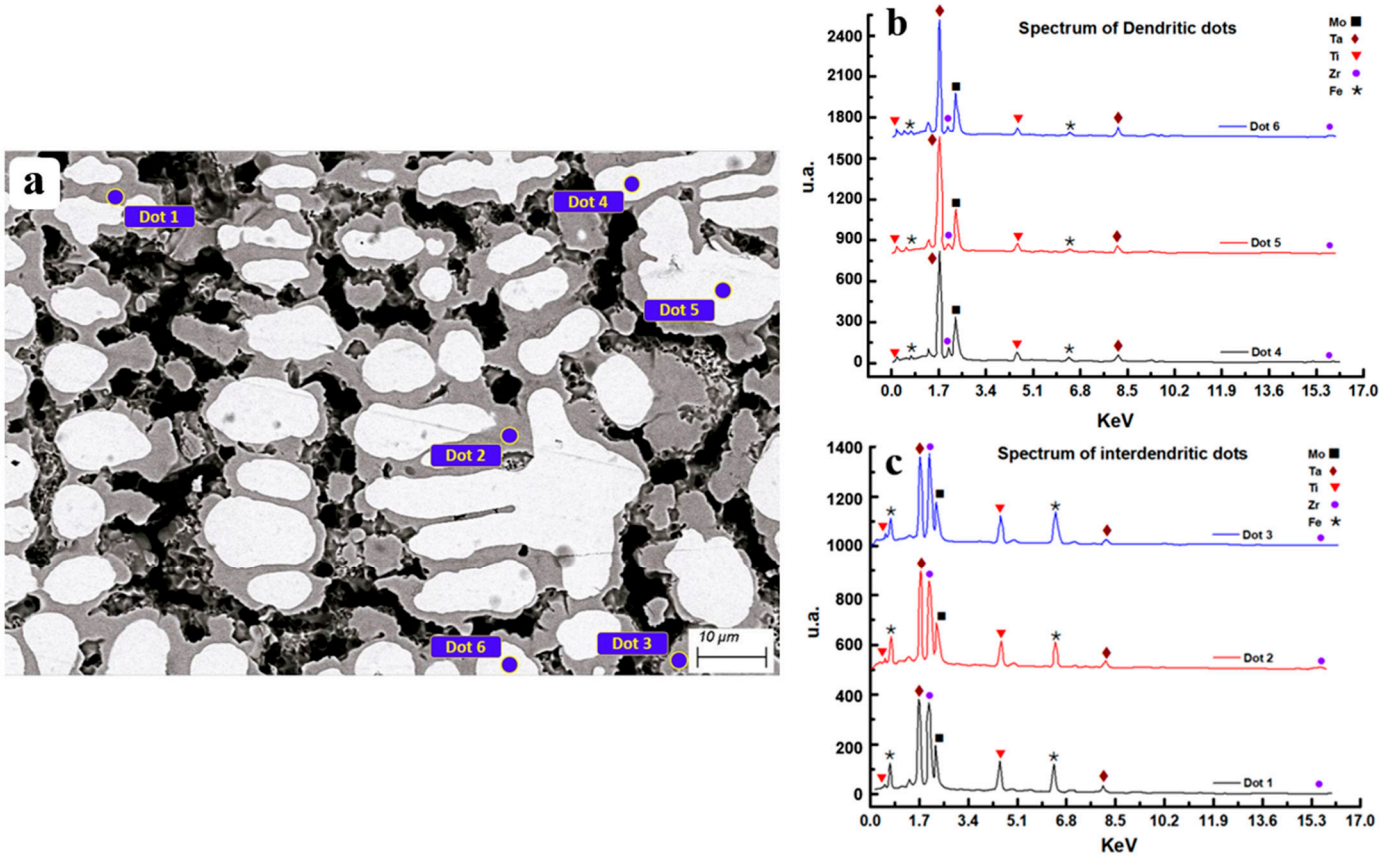

Figure 3. (**a**) SEM and EDS analysis for Area 1, Area 2, and Area 3 of FeMoTaTiZr high-entropy alloy; (**b**) compositional spectrum in dendritic areas; (**c**) compositional spectrum in interdendritic areas.

Table 5. EDS quantification results of atomic and weight percentage on dendritic (D) and interdendritic (ID) microstructures of FeMoTaTiZr high-entropy alloy.

Spot	1		2		3		4		5		6	
	ID		ID		ID		D		D		D	
Elements	**wt %**	**at %**	**wt %**	**at %**	**wt %**	**at %**	**wt %**	**at %**	**wt %**	**at %**	**wt %**	**at %**
Ti	10.58	18.18	10.81	18.48	11.14	18.54	9.14	18.09	7.61	15.97	7.60	15.85
Fe	14.68	21.62	14.78	21.65	16.50	23.54	5.24	8.89	3.30	5.94	3.41	6.10
Zr	37.44	33.77	36.07	32.34	39.38	34.41	9.47	9.83	3.51	3.86	4.35	4.76
Mo	23.51	20.16	25.45	21.70	23.03	19.13	50.27	49.64	54.29	56.85	54.32	56.55
Ta	13.79	6.27	12.89	5.83	9.95	4.38	25.88	13.55	31.29	17.38	30.32	16.74

Table 6. Composition average results in dendritic (D) and interdendritic (ID) areas and S_R values for FeHEA and NbHEA.

	Parameters	Ti	Zr	Mo	Ta	Nb	Fe
FeHEA	D	8.12	5.78	52.96	29.19	-	3.98
	ID	10.84	37.63	24.00	12.21	-	15.32
	S_R	0.75	0.15	2.21	2.39	-	0.26
NbHEA	D	7.19	8.04	18.51	54.43	9.86	-
	ID	17.10	35.45	8.18	29.65	9.64	-
	S_R	0.42	0.23	2.26	1.84	1.02	-

For the analysed samples, the distribution of the constituents inside the dendrite, so as through the inter-dendrite areas, shows that all the composing elements are contained in

both regions. This is consistent with the formation of multicomponent solid solution phases. For the NbHEA, a phase in the main-dendrite region is enriched with Ta, Nb, and Mo, and a minor phase the inter-dendrite region accumulates higher Ti and Zr concentrations.

The distribution of the constituents can be described with the enthalpy of mixing, attending to the high-melting-temperature elements (Mo, Nb, and Ta). During the solidification process, the dendrite phase is formed. Nb, Mo, and Ta are elements with high melting temperature, which forces Ti and Zr to be expelled from the phase as a consequence of the positive values of the enthalpy of mixing for the different combinations Ta-Zr, Ta-Ti, Nb-Zr, and Nb-Ti. This results in the enrichment of the inter-dendrite region with Ti and Zr. The enthalpy and miscibility between the different atoms in the solution phase of HEA are intrinsically linked to the partitioning of elements [10].

For the FeHEA, the main-dendrite region is also supported with Ta and Mo, and the inter-dendrite region also contains Ti and Zr, as explained for the NbHEA. However, Fe is now also added to the inter-dendrite region, showing a much higher tendency to be expelled from the dendrite than Nb. Again, high-melting-temperature elements keep a tendency to occupy dendrite phases. Following the former, Ti and Zr (in both alloys), and now also Fe, show segregation factors with a lower value than the unit, which make them the main constituents of the inter-dendrite regions. Additionally, the shift in the segregation factor values indicates that with the addition of Fe instead of Nb, dendrite regions' compositions are reinforced with Ta and Ti, while Mo proportions keep mainly steady. The microstructure and composition of cast FeMoTaTiZr high-entropy alloy, with dendrites based on Mo and Ta, dispersed in Ti, Fe, and Zr matrix [26], are in agreement with the results obtained in this study.

3.2. Corrosion Tests

3.2.1. Open Circuit Potential (OCP)

Open circuit potential measurement curves during 24 h immersion for both NbHEA and FeHEA are shown in Figure 4.

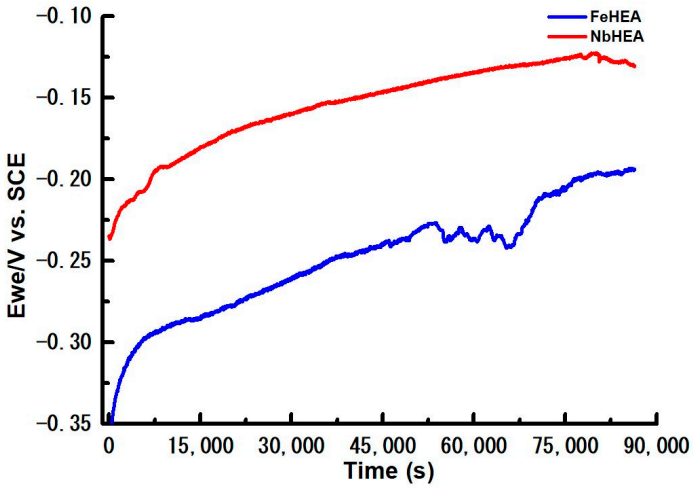

Figure 4. Open circuit potential variation with time for the two samples FeHEA and NbHEA in Ringer solution.

The open circuit potential (OCP) of metallic samples refers to the voltage difference between a reference electrode and a metal sample when there is no external current flowing between them. The OCP of a metal depends on its electrochemical properties, such as its standard electrode potential. Metals with higher standard electrode potentials tend to have more positive OCP values compared to those with lower standard electrode potentials. This is because metals with higher electrode potentials have a greater tendency to lose electrons and undergo oxidation, resulting in a more positive potential. The chemical composition of the metal, particularly the presence of alloying elements, can influence its electrochemical

behavior and, consequently, its OCP. Niobium has a relatively cathodic standard electrode potential of ca. −1 V vs. standard hydrogen electrode (SHE) ($E^0_{Nb/Nb3+} \sim -1.1$ V and $E^0_{Nb/Nb5+} \sim -0.96$ V) while iron has $E^0_{Fe/Fe2+} \sim -0.45$ V vs. SHE. It can be observed that the OCP for both samples are shifting to more positive values during the immersion time (see Figure 4). The variation of open circuit potential (OCP) to more positive values during the time of immersion can be explained by several factors related to the electrochemical behavior of the metallic sample in the Ringer solution. Both studied alloys develop a passive oxide layer on their surface during the immersion, and this passive film acts as a barrier that reduces the rate of corrosion by preventing direct contact between the metal and corrosive agents. As the passive film forms and stabilizes, it causes the OCP to shift to more positive values. This shift indicates that the alloys are becoming more passive and less reactive towards corrosion. In aqueous Ringer environments, oxygen reduction reactions occur on the surface of metals, leading to the consumption of dissolved oxygen in the solution. As the concentration of oxygen decreases near the metal surface, the OCP tends to shift to more positive values due to the decrease in the cathodic reaction rate. The oscillations (increasing and decreasing) of OCP for FeHEA sample can be explained by the depassivation process, which occurs when the passive layer breaks down, causing a decrease in OCP, but after it, the stable passive layer forms again, leading to an increase in OCP.

3.2.2. Potentiodynamic Polarization

Following the potentiodynamic polarization, plots in a semi-logarithmic version are displayed in Figure 5.

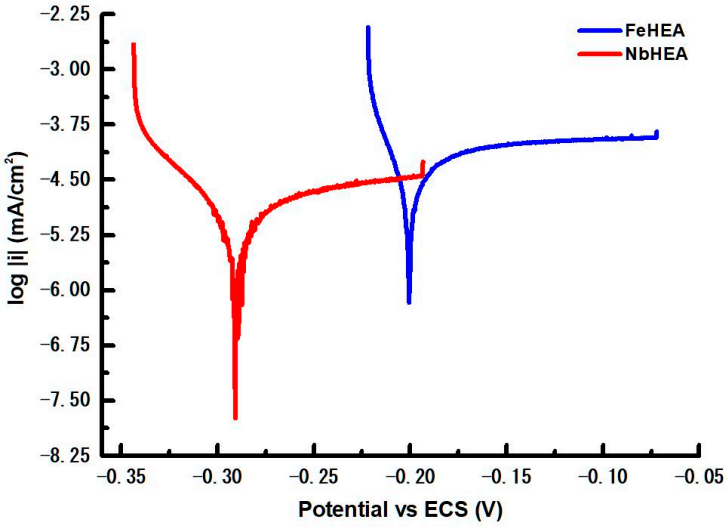

Figure 5. Tafel curves for the two samples of FeHEA and NbHEA after 24 h immersion in Ringer solution.

Potentiodynamic polarization is a widely used electrochemical technique for studying the corrosion behavior of metallic materials. When potentiodynamic polarization data were plotted in a semi-logarithmic version (i.e., with the logarithm of the current density on the *y*-axis), several corrosion parameters can be obtained: corrosion potential, corrosion current density, Tafel slopes, and corrosion rate. By using EC-Lab® software, the analytic results of E_{corr}, i_{corr}, b_a, b_c, and V_{corr} are presented in Table 7.

It can be observed (see Table 7) that FeHEA, with the higher corrosion current, is experiencing more corrosion or corroding at a faster rate. This is due to factors such as passivation and the formation of a less protective oxide layer, all of which contribute to deteriorating the corrosion resistance. The dissolution of Fe in the Ringer Grifols solution was associated with the anodic portion of the polarization curve (above E_{corr}), whereas the cathodic region (below E_{corr}) was associated with the cathodic reaction of oxygen. E_{corr} of

NbHEA presents a more negative (active) potential value compared to that of FeHEA by −90 mV, whereas the corrosion current density (I_{corr}) shows a growth from 10 nA cm^{-2} to 39 nA cm^{-2}. The rate of degradation for the FeHEA was probably accelerated by substitution of Nb with Fe, and the average of the degradation rate (mmpy) became almost four times higher for FeHEA than for NbHEA. The corrosion current density of FeHEA is comparable with that of Ti6Al4V [27].

Table 7. Electrochemical parameters estimated through Tafel approximation.

	E_{corr}	i_{corr}	b_c	b_a	V_{corr}
	mV	**μA·cm^{-2}**	**mV dec^{-1}**	**mV dec^{-1}**	**mmpy**
FeHEA	−200.51	0.039	26.90	202.10	4.9×10^{-4}
NbHEA	−290.78	0.010	45.50	325.50	1.3×10^{-4}

3.2.3. Electrochemical Impedance Spectroscopy (EIS)

Electrochemical impedance spectroscopy (EIS) is a powerful technique for analyzing corrosion processes due to its ability to provide detailed information about the electrochemical behavior of metallic systems. EIS can provide insight into the kinetics of corrosion processes by analyzing impedance data over a range of frequencies. Changes in impedance spectra, such as the shape and position of impedance arcs, can reveal information about the corrosion rate, corrosion mechanism, and the formation of passive films or corrosion products.

The Nyquist representation of the EIS analysis is displayed in Figure 6. Both the FeHEA and NbHEA samples, in the high-to-low frequency region, display a semicircle formation. There is a direct correspondence between the semicircular portion of a Nyquist plot and the limited process of electron transfer at the metal surface through the solution interface. For the corrosion process, the diameter of these semicircles can be used to interpret the electron transfer resistance. It is clear, when comparing the two Nyquist plots, that an important reduction of the electron transfer resistance is shown for the FeHEA sample, which indicates that the substitution of Nb with Fe produced an acceleration of the corrosion rate for this FeHEA.

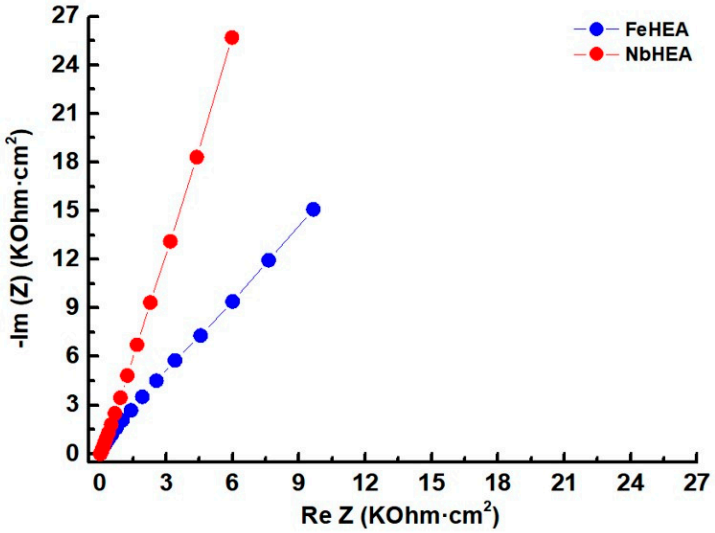

Figure 6. Nyquist vs. Eocp curves for the two samples of FeHEA and NbHEA.

In the Bode-Z plots shown in Figure 7, overlapping curves are formed for the range of frequency displayed. It can be observed that the impedance of both HEA improved linearly with decreasing frequency in the range of 10^3–10^{-1} Hz, indicating that the passive film on the samples surface have optimal corrosion resistance.

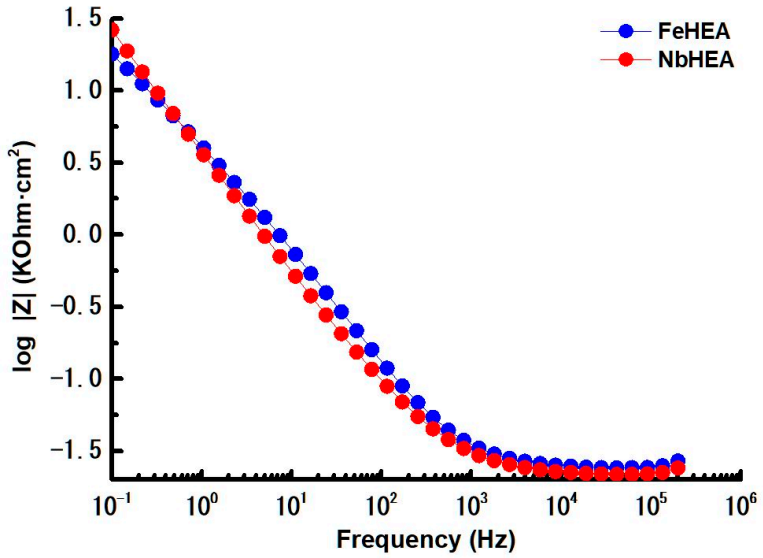

Figure 7. Bode Z vs. Eocp curves for the two samples of FeHEA and NbHEA.

For the open circuit potential versus the Reference electrode, the phase displacement in proportion to frequency is displayed via the Bode-phase plot in Figure 8. It can be observed from the curves that theta changes in a more significant way in the low-frequency region for the FeHEA. At low frequencies, the system has increased time to equilibrate, allowing electrochemical processes to predominate the impedance response. The phase angle diminishes due to the presence of a resistive component in these processes, which mitigates the overall capacitive phase shift. The diffusion of ions to and from the alloy surface in simulated human fluid is constrained by mass transport restrictions. At low frequencies, imperfections or ion diffusion within the passive layer may become prominent, affecting the phase angle and leading to its reduction.

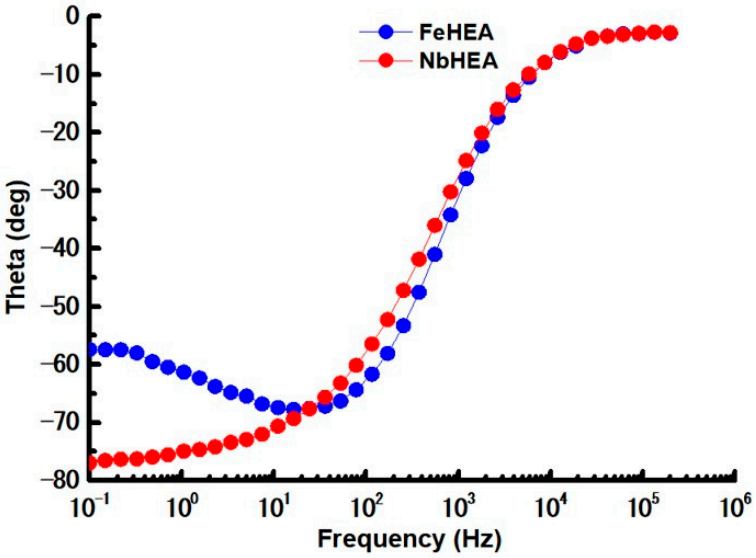

Figure 8. Bode Theta vs. Eocp curves for the two samples of FeHEA and NbHEA.

When considering metals to be inside the human body, those with an electrode potential slightly higher than zero may be degraded. Degradation process and the grade of the corrosion kinetics are influenced by characteristics of the inner human body environment (e.g., flow and pH). Another specific parameter to take into account is the surface film condition.

In the physiological conditions, the electrochemical deportment of HEA occurs in an oxygen absorption mode, increasing the pH value of the solution, and can be expressed through the following reactions:

$$\text{Anodic reaction: Me} \rightarrow \text{Mex}^{+} + \text{xe}^{-} \quad (4)$$

$$\text{Cathodic reaction: } O_2 + 2H_2O + 4e^{-} \rightarrow 4OH^{-} \quad (5)$$

During the anodic oxidation, the passive film is predominantly formed by stable oxides such as: TiO_2, ZrO_2, MoO_3, MoO_2, and Ta_2O_5. In the case of NbHEA, the passive film also contains Nb_2O_5. In the case of FeHEA, the iron reactions in physiological conditions (pH = 7.4 and T = 37 °C) with the corresponding enthalpy calculated with common Standard Enthalpy of Formation values [28] are:

$$Fe \rightarrow Fe^{2+} + 2e^{-} \quad \Delta H = -87.9 \text{ kJ/mol} \quad (6)$$

$$Fe^{2+} + 2OH^{-} \rightarrow Fe(OH)_2 \quad \Delta H = +57.9 \text{ kJ/mol} \quad (7)$$

$$Fe^{2+} \rightarrow Fe^{3+} + e^{-} \quad \Delta H = +40.2 \text{ kJ/mol} \quad (8)$$

$$Fe^{3+} + 3OH^{-} \rightarrow Fe(OH)_3 \quad \Delta H = -2.3 \text{ kJ/mol} \quad (9)$$

The proposed equilibrium equations are shown in equations:

$$Fe(OH)_2 + Cl^{-} \rightarrow FeClOH + OH^{-} \quad (10)$$

$$FeClOH + H^{+} \rightarrow Fe^{2+} + Cl^{-} + H_2O \quad (11)$$

$$Fe^{2+} + O_2 + 3OH^{-} \rightarrow Fe(OH)_3\downarrow + O^{2-} \quad (12)$$

$$Fe(OH)_3 + 2Cl^{-} \rightarrow FeCl_2OH + 2OH^{-} \quad (13)$$

Chloride ions have been identified in solid intermediate species during the precipitation of Fe(III) hydroxide from aqueous chloride solutions, suggesting that this species is stable in weakly acidic solutions with low chloride concentrations. Nonetheless, the stability of FeClOH and $FeCl_2OH$, if it indeed exists, is minimal, and these species are not regarded as significant [29].

Both the electrochemical oxidation and reduction of iron in the presence of oxygen and the stability conditions of compounds that may originate in processes involving the gaseous phase have been examined [30]. Fe is particularly prone to selective dissolution due to the low stability of iron species in comparison to other species.

For additional EIS data interpretation, an analogous electric circuit is proposed. A precise fit and interpretation of EIS data depend on the correct choice of the circuit. In addition to being as simple as possible while retaining the key elements of the system, it is a requisite that the equivalent circuit is physically meaningful and pertinent to the electrochemical system under study.

The corrosion process characteristics were modelled using the equivalent circuit depicted in Figure 9, pretending to be a suitable compromise between physical significance and simplicity based on the impedance. The electrolyte resistance is presented as R_e in the figure. Capacitance Q_p and resistance R_p represent the impedance of the pores. It is supposed to be in the passive film, strongly involved with the conduction of ions through the passive layer structure. This gives an idea of the protection level that the passive film can represent for the base alloy when facing corrosion. Finally, both the capacitance Q_c and the resistance R_c stand for the polarization resistance at the interface between the alloy and passive film, since the electrolyte is thought to enter into the pores.

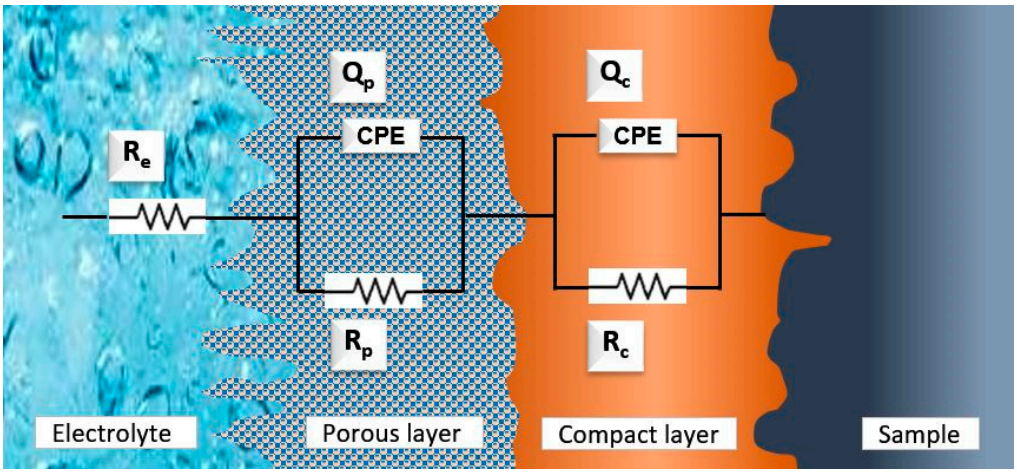

Figure 9. Equivalent circuit used for the EIS experimental data and its interpretation in the interface for the two samples of FeHEA and NbHEA.

ZSimpWin 3.60 software was utilized to analyze the impedance spectra. Data were computed to assess the fit quality by contrasting the simulated and experimental data [31]. The equivalent circuit impedance can be calculated with the following equation:

$$Z = R_e + \frac{R_p}{1 + R_p Y_p (jw)^{n_p}} + \frac{R_c}{1 + R_c Y_c (jw)^{n_c}} \quad (14)$$

The value of the different parameters is displayed in Table 8.

Table 8. Parameter values of the equivalent circuit for FeHEA and NbHEA.

	R_c	Y_c	n_c	R_p	Y_p	n_p	R_e
	[Ω·cm^2]	[S·s^n cm^{-2}]	-	[Ω·cm^2]	[S·s^n cm^{-2}]	-	[Ω·cm^2]
FeHEA	24.37	1.00×10^{-4}	0.7950	2.77×10^{3}	$7.99 \cdot 10^{-5}$	0.8183	8.91×10^{4}
NbHEA	27.78	7.37×10^{-5}	1	5.72×10^{5}	$1.47 \cdot 10^{-4}$	0.7117	1.39×10^{4}

Since the distance between the working electrode and the reference electrode affects the resistance of the electrolyte R_e, it was aimed to be constant in both experiments. The pores' resistance in the passive film can be deducted from R_p and Y_p values, which show lower values for the FeHEA, indicating a likely higher ion conduction through the structure of the passive film. The n factor gives an idea of the proximity of the Y variable to the capacitor behavior, where similar n-values can be seen for both samples. A higher ability of the electrolyte to enter into the pores of the FeHEA can be fathomed. Finally, a lower polarization resistance can be seen through R_c values, referring to the interface between the passive film and the base alloy.

3.3. Microhardness

Imprints measurement is used to obtain Vickers Hardness. The results for the two samples are plotted in Figure 10.

For the NbHEA, an average value of 496.70 kgf·mm^{-2} is obtained, with a standard deviation of 17.72 kgf·mm^{-2}. For the FeHEA, an average value of 628.80 kgf·mm^{-2} is obtained, with a standard deviation of 24.13 kgf·mm^{-2}.

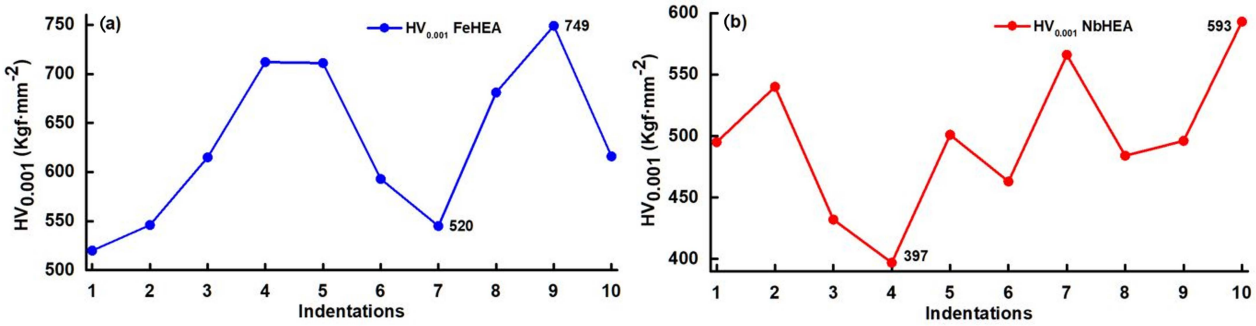

Figure 10. $HV_{0.01}$ microhardness test results for sample of (**a**) FeHEA and (**b**) NbHEA.

No big difference is shown between the two samples, though FeHEA exhibits higher microhardness results than NbHEA. Changes in the material structure process may be caused by the cutting process, enabling the formation of thin layers of altered material. These layers may influence the results. Also, the corrosion layers' formation can affect the hardness values when using low loads. Efforts were made to minimize those effects through additional polishing of the samples. Hardness values are similar for both samples, showing higher results for the FeHEA. This level qualifies the alloy for the manufacture of medical devices subjected to high mechanical stress.

4. Conclusions

In the present study, two different samples of HEAs MoNbTaTiZr and FeMoTaTiZr were analyzed. Both samples were produced with electric-arc remelting technology at a laboratory. The alloys were formed keeping similar atomic percentage of the elements in both alloys. Optical microscopy and scanning electron microscopy techniques were used to characterize the microstructure of the alloys. Replacing Nb with Fe has an influence on the layout proportion of the other four elements, with Fe leaving the dendrite towards the inter-dendrite region, whereas Nb has a tendency to stay in both regions. As for the corrosion properties, the synthesized alloys showed some differences. Both samples were evaluated under simulated biological environment using the potentiodynamic polarization method and electrochemical impedance spectroscopy (EIS). The tests proved that FeHEA has a higher corrosion rate than NbHEA. Both alloys represented by the same equivalent electrical circuit allows us to propose that the similar composition of those two alloys let them show similar corrosion products and layers formation. But the influence of the lower stability of the iron species offers a selective dissolution that probably increases the corrosion rate of the FeHEA compared to the NbHEA. In order to better characterize the FeHEA corrosion behavior, further studies focused on this matter should be aimed. Taking this into account, it would also be interesting to perform further microhardness tests on corroded samples so that the influence of iron corrosion effects on the hardness can be better analyzed.

Author Contributions: M.L.-R.: investigation, methodology and conceptualization, writing of the original draft; S.B.-G.: investigation, methodology, writing—review and editing; I.V.: investigation (Table 1) and review of the writing; J.M.-R.: data validation, project administration, visualization, review and editing. All authors have read and agreed to the published version of the manuscript.

Funding: This research received no external funding.

Data Availability Statement: The original contributions presented in this study are included in the article. Further inquiries can be directed to the corresponding author.

Acknowledgments: We hereby acknowledge the project "The Smart Healthcare Engineering (SHEng)", with number 2023-1-RO01-KA220-HED-000159985, co-funded by the European Union.

Conflicts of Interest: The authors declare no conflicts of interest.

References

1. Cantor, B.; Chang, I.; Knight, P.; Vincent, A.J.B. Microstructural Development in Equiatomic Multicomponent Alloys. *Mater. Sci. Eng. A* **2004**, *375–377*, 213–218. [CrossRef]
2. Li, D.; Liaw, P.K.; Xie, L.; Zhang, Y.; Wang, W. Advanced High-Entropy Alloys Breaking the Property Limits of Current Materials. *J. Mater. Sci. Technol.* **2024**, *186*, 219–230. [CrossRef]
3. Yeh, J.-W. Recent Progress in High-Entropy Alloys. *Ann. Chim. Sci. Mat.* **2006**, *31*, 633–648. [CrossRef]
4. Miracle, D.; Senkov, O. A Critical Review of High Entropy Alloys and Related Concepts. *Acta Mater.* **2016**, *122*, 448–511. [CrossRef]
5. Tsai, M.; Yeh, J.-W. High-Entropy Alloys: A Critical Review. *Mater. Res. Lett.* **2014**, *2*, 107–123. [CrossRef]
6. Rosca, J.; Santana, E.D.; Castro, J.; Lopez, A.; Vasilescu, E.V.; Drob, P.; Vasilescu, C. Characterisation of Anodic Films Formed on Titanium and Its Alloys. *Mater. Corros.* **2005**, *56*, 692–696. [CrossRef]
7. Jimenez-Marcos, C.; Mirza-Rosca, J.C.; Baltatu, M.S.; Vizureanu, P. Experimental Research on New Developed Titanium Alloys for Biomedical Applications. *Bioengineering* **2022**, *9*, 686. [CrossRef]
8. Baltatu, M.S.; Spataru, M.C.; Verestiuc, L.; Balan, V.; Solcan, C.; Sandu, A.V.; Geanta, V.; Voiculescu, I.; Vizureanu, P. Design, Synthesis, and Preliminary Evaluation for Ti-Mo-Zr-Ta-Si Alloys for Potential Implant Applications. *Materials* **2021**, *14*, 6806. [CrossRef]
9. Surmeneva, M.; Grubova, I.; Glukhova, N.; Khrapov, D.; Koptyug, A.; Volkova, A.; Ivanov, Y.; Cotrut, C.M.; Vladescu, A.; Teresov, A.; et al. New Ti–35Nb–7Zr–5Ta Alloy Manufacturing by Electron Beam Melting for Medical Application Followed by High Current Pulsed Electron Beam Treatment. *Metals* **2021**, *11*, 1066. [CrossRef]
10. Todai, M.; Nagase, T.; Hori, T.; Matsugaki, A.; Sekita, A.; Nakano, T. Novel TiNbTaZrMo High-Entropy Alloys for Metallic Biomaterials. *Scr. Mater.* **2017**, *129*, 65–68. [CrossRef]
11. Senkov, O.; Wilks, G.; Miracle, D.; Chuang, C.; Liaw, P. Refractory High-Entropy Alloys. *Intermet. Barking* **2010**, *18*, 1758–1765. [CrossRef]
12. Lin, S.; Lai, W.; Vogel, F.; Tong, X.; You, D.; Li, W.; Wang, X. Mechanical and Corrosion Properties of Biomedical (TiZr)90-XNbxTa5Mo5 Medium Entropy Alloys. *Int. J. Refract. Metals Hard Mater.* **2023**, *116*, 106361. [CrossRef]
13. Hanawa, T. Metal Ion Release from Metal Implants. *Mater. Sci. Eng. C* **2004**, *12*, 745–752. [CrossRef]
14. Akmal, M.; Park, H.-K.; Ryu, H.J. Plasma Spheroidized MoNbTaTiZr High Entropy Alloy Showing Improved Plasticity. *Mater. Chem. Phys.* **2021**, *273*, 125060. [CrossRef]
15. Günen, A.; Ceritbinmez, F.; Patel, K.; Akhtar, M.A.; Mukherjee, S.; Kanca, E.; Karakas, M.S. WEDM Machining of MoNbTaTiZr Refractory High Entropy Alloy. *CIRP J. Manuf. Sci. Technol.* **2022**, *38*, 547–559. [CrossRef]
16. Matsuno, H.; Yokoyama, A.; Watari, F.; Uo, M.; Kawasaki, T. Biocompatibility and Osteogenesis of Refractory Metal Implants, Titanium, Hafnium, Niobium, Tantalum and Rhenium. *Biomaterials* **2001**, *22*, 1253–1262. [CrossRef] [PubMed]
17. Ishimoto, T.; Ozasa, R.; Nakano, K.; Weinmann, M.; Schnitter, C.; Stenzel, M.; Matsugaki, A.; Nagase, T.; Matsuzaka, T.; Todai, M.; et al. Development of TiNbTaZrMo Bio-High Entropy Alloy (BioHEA) Super-Solid Solution by Selective Laser Melting, and Its Improved Mechanical Property and Biocompatibility. *Scr. Mater.* **2021**, *194*, 113658. [CrossRef]
18. Gąsior, G.; Szczepański, J.; Radtke, A. Biodegradable Iron-Based Materials—What Was Done and What More Can Be Done? *Materials* **2021**, *14*, 3381. [CrossRef] [PubMed]
19. *ASTM E3-11*; Standard Guide for Preparation of Metallographic Specimens. ASTM International: West Conshohocken, PA, USA, 2017.
20. *Designation: G 5-87*; Standard Reference Test Method for Making Potentiostatic and Potentiodynamic Anodic Polarization Measurements. ASTM International: West Conshohocken, PA, USA, 2003.
21. *ASTM G 102-89*; ASTM-Standards Standard Practice for Calculation of Corrosion Rates and Related Information from Electrochemical Measurements. ASTM International: West Conshohocken, PA, USA, 1999; Volume 89, pp. 1–7.
22. *ISO 16773-1-4*; Electrochemical Impedance Spectroscopy (EIS) on Coated and Uncoated Metallic Specimens. ISO: Geneva, Switzerland, 2016.
23. *ISO 14577-1*; Metallic Materials—Instrumented Indentation Test for Hardness and Materials Parameters—Part 1: Test Method. ISO: Geneva, Switzerland, 2015.
24. Hori, T.; Nagase, T.; Todai, M.; Matsugaki, A.; Nakano, T. Development of Non-Equiatomic Ti-Nb-Ta-Zr-Mo High-Entropy Alloys for Metallic Biomaterials. *Scr. Mater.* **2019**, *172*, 83–87. [CrossRef]
25. de Oliveira, T.G.; Fagundes, D.; Capellato, P.; Sachs, D.; da Silva, A.A.A.P. A Review of Biomaterials Based on High-Entropy Alloys. *Metals* **2022**, *12*, 1940. [CrossRef]
26. Codescu, M.; Vladescu, A.; Geanta, V.; Voiculescu, I.; Pana, I.; Dinu, M.; Kiss, A.; Braic, V.; Patroi, D.; Virgil, M.; et al. Zn Based Hydroxyapatite Based Coatings Deposited on a Novel FeMoTaTiZr High Entropy Alloy Used for Bone Implants. *Surf. Interfaces* **2021**, *28*, 101591. [CrossRef]
27. Kovacı, H.; Şenel, K.; Acar, T.; Bozkurt, Y.; Çelik, A. Comparative Investigation of Structural, Morphological, Mechanical, Tribological and Electrochemical Properties of TiO2 Films Formed on Cp-Ti, Ti6Al4V and Ti45Nb Alloys. *Surf. Coat. Technol.* **2024**, *487*, 131024. [CrossRef]
28. Lemire, R.; Berner, U.; Musikas, C.; Palmer, D.; Taylor, P.; Tochiyama, O. *Chemical Thermodynamics of Iron, Chemical Thermodynamics, Part 1*; OECD Nuclear Energy Agency: Seine Saint-Germain, France, 2013; No. 6355.

29. Waite, T.D. Chapter 7. Thermodynamics of the Iron System in Seawater. In *The Biochemistry of the Iron System in Seawater*; Turner, D.R., Hunter, K.A., Eds.; John Wiley and Sons, Ltd.: Hoboken, NJ, USA, 2001; pp. 292–340.
30. Pourbaix, M.; Zhang, H.; Pourbaix, A. Presentation of an Atlas of Chemical and Electrochemical Equilibria in the Precence of a Gaseous Phase. *Mater. Sci. Forum* **1997**, *251*, 143–148. [CrossRef]
31. Boukamp, B.A. A Nonlinear Least Squares Fit Procedure for Analysis of Immittance Data of Electrochemical Systems. *Solid. State Ion.* **1986**, *20*, 31–44. [CrossRef]